Research Article | Vol. 28, No. 11 / 25 May 2020 / Optics Express 15874

Optics EXPRESS

Generation of isolated circularly polarized attosecond pulses by three-color laser field mixing

RENZHI SHAO,[1,3] CHUNYANG ZHAI,[1,3] YINFU ZHANG,[1] NING SUN,[1] WEI CAO,[1] PENGFEI LAN,[1,*] AND PEIXIANG LU[1,2]

[1] *Wuhan National Laboratory for Optoelectronics and School of Physics, Huazhong University of Science and Technology, Wuhan 430074, China*
[2] *Hubei Key Laboratory of Optical Information and Pattern Recognition, Wuhan Institute of Technology, Wuhan 430205, China*
[3] *These authors contributed equally to this work*
[*] *pengfeilan@hust.edu.cn*

Abstract: We propose and theoretically demonstrate a method to generate the circularly polarized supercontinuum with three-color electric fields. The three-color field is synthesized from an orthogonally polarized two-color (OTC) laser field and an infrared gating field. All driving pulse durations are extended to 40 fs. We demonstrate that the three-color field imposes curved trajectories for ionized electrons and extends the time interval between each harmonic emitting. Through adjusting intensity ratios among three components of the driving field, a nearly circular isolated attosecond pulse can be generated.

1. Introduction

The circularly polarized attosecond pulses impart numerous applications to the ultrafast measurement in physics, chemistry, biology and materialogy [1–5]. They are demonstrated as a promising way to characterize the chirality of atoms and molecules, magnetic circular dichroism and angular momentum of atomic orbitals [6–8]. The high-order harmonic generation (HHG) process driven by femtosecond lasers is an established way to produce the attosecond bursts [9,10]. Many methods have been proposed to generate linearly polarized isolated attosecond pulses, such as few-cycle driving lasers [11] and polarization gating (PG) [12]. Especially, multi-cycle pulses can be used in the two-color laser fields [13], double optical gating (DOG) [14] and generalized double optical gating (GDOG) method [15]. Since the HHG yield descends rapidly as the driving fields become circularly polarized, it is difficult to generate the HHG with high ellipticity.

At first, multi-reflection phase retarders are employed to convert the linear polarization of harmonics into circular polarization, but their poor reflectivity and narrow bandwidth restrict this method for many applications [16,17]. In recent works, many schemes have been developed to generate circular attosecond pulses [18–21]. Most of scenarios can be separated into two types – collinear schemes and non-collinear schemes. The collinear schemes employ the combination of two laser fields along an overlapping propagation axis, such as two counterrotating circularly polarized laser fields which generate bicircular high-order harmonics [3,22–25]. Due to the n-fold ($n \geq 3$) rotational symmetry of two-color circularly polarized laser field [26], the HHG always has opposite helicity for neighbored orders. The opposite helicity of harmonics inhibits generating circularly polarized attosecond pulses. Therefore, the helicity of attosecond pulses have to be controlled by adding external conditions such as changing the intensity ratio between two driving fields or using aligned molecules as interacting media [27–35].

On the other hand, two laser beams with a tiny crossing angle of propagation axis are combined in the non-collinear schemes. An example is two non-collinear counter-rotating (NCP) laser beams

#388480 https://doi.org/10.1364/OE.388480
Journal © 2020 Received 17 Jan 2020; revised 30 Apr 2020; accepted 1 May 2020; published 13 May 2020

Optics EXPRESS

with the same frequency, generating angularly separated circularly polarized high harmonics with different helicity in the far-field [6,19,36]. According to the peculiarity of angularly separated harmonics, it is possible to generate attosecond pulses of pure circular polarization with the NCP driving field. However, non-collinear schemes are so far restricted to the lower flux due to limited interacting region [19]. In addition to those two schemes, the collinear superposition of two independent, phase-locked, orthogonally polarized extreme-ultraviolet sources also is utilized to produce circularly polarized high harmonics, but this method requires the control of their relative delay with sub-cycle accuracy [37]. To generate the isolated attosecond pulse with high ellipticity, all driving laser fields of those aforementioned schemes have to be few-cycle, which demands sophisticated and robust upstream femtosecond laser setup in experiments.

In this paper, we propose and demonstrate a scheme to generate circularly polarized high harmonics supercontinuum with a three-color linearly-polarized laser field. Different from the traditional schemes, this scheme works for multi-cycle driving lasers. The pulse duration of all driving fields can be extended to 40 fs. The generated supercontinuum from the multi-cycle driving pulses is employed to generate an isolated attosecond pulse with high ellipticity. Furthermore, we investigate the dependence of the harmonic ellipticity on driving field parameters and show the robustness of the HHG with the three-color field.

2. Theoretical model

As in Ref. [20], we apply the strong-field approximation (SFA) to numerically calculate the HHG of the three-color fields [38–40]. It has been proved that the HHG of SFA calculations agrees qualitatively with that of the time-dependent Schrödinger equation (TDSE) [41]. And we confirmed the validity of our scheme in TDSE calculations as well. The driving laser field is consisting of an OTC electric field and an infrared (IR) gating field. The interacting atom is neon, which has an isotropic $2p$ orbital. Since the electron dynamics mainly occur in polarization plane of the electric field, we employ the spherical-basis representation of the three degenerate ($2p$) orbitals of neon: $p_\pm = \frac{1}{\sqrt{2}}(p_x \pm i p_y), p_0 = p_z$. The contribution of the p_0 orbital to HHG is neglected because the p_0 orbital only has a node in the polarization plane. According to the SFA, the time-dependent dipole momentum $\boldsymbol{x}(t)$ is described as (atomic units are used throughout this paper unless otherwise mentioned)

$$\begin{aligned}\boldsymbol{x}(t) = i\int_{-\infty}^{t} \mathrm{d}t' \left[\frac{\pi}{\xi + i\,(t-t')\,/2}\right]^{3/2} \times \boldsymbol{d}\left[\boldsymbol{p}_s\,(t',t) - \boldsymbol{A}\,(t')\right] \boldsymbol{d}^*\left[\boldsymbol{p}_s\,(t',t) - \boldsymbol{A}(t)\right] \\ \times e^{-iS(t',t)}\boldsymbol{E}\,(t')\,g\,(t') + \text{c.c.}\end{aligned} \tag{1}$$

where $\boldsymbol{E}(t)$ is the electric field, $\boldsymbol{A}(t) = -\int_{-\infty}^{t} \boldsymbol{E}(t')dt'$ is corresponding vector potential, ξ is a positive regularization constant and $\xi = 10^{-5}$ is used in calculation, $\boldsymbol{d}^*[\boldsymbol{p}_s(t,t') - \boldsymbol{A}(t)]$ and $\boldsymbol{d}[\boldsymbol{p}_s(t,t') - \boldsymbol{A}(t)]$ denote the transition dipole matrix element for photoionization and photorecombination process in length gauge respectively, $\boldsymbol{p}_s$ represents the stationary momentum, $S = \int_{t'}^{t}\left[\frac{1}{2}(\boldsymbol{p}_s - \boldsymbol{A}(t))^2 + I_p\right] dt'' - \Omega t$ indicates the quasiclassical action with ionization potential I_p and the fundamental frequency Ω, $g(t')$ is the ground-state probability. In SFA calculation, the HHG is expected to be dominated by the transitions between the ground state and continuum states. This approximation is valid due to the negligible ionization fraction of $2p$ orbital in our scheme. Then, to analyze the HHG, we calculate the electron dipole acceleration $\ddot{\boldsymbol{x}}(t)$ as the second derivative of the time-dependent dipole momentum and process Fourier transform of $\ddot{\boldsymbol{x}}(t)$ to obtain the harmonic electric field $\boldsymbol{E}_q$ in frequency-domain. Finally, the high harmonic intensity can be obtained by $I_q = |\boldsymbol{E}_q|^2$. The ellipticity of the harmonics can be calculated as $\epsilon = (|\boldsymbol{a}_+| - |\boldsymbol{a}_-|)/(|\boldsymbol{a}_+| + |\boldsymbol{a}_-|)$ in which $\boldsymbol{a}_\pm = \frac{1}{\sqrt{2}}(\boldsymbol{a}_x \pm i\boldsymbol{a}_y)$. The $\boldsymbol{a}_x$ and $\boldsymbol{a}_y$ are the x, y components of the harmonic spectrum, respectively. The sign of the harmonic ellipticity describes the helicity

Optics EXPRESS

of the harmonics. In addition, the harmonic spectrum can be projected into two counter-rotating components, i.e. right circularly polarized (RCP) harmonics $D_+ = |\boldsymbol{a}_+|^2$ and left circularly polarized (LCP) harmonics $D_- = |\boldsymbol{a}_-|^2$.

To analyze the contribution of electron dynamic process to the harmonic spectrum, we solve the saddle-point equations over the two observable variables t_s', t_s [42–45]:

$$\mathbf{v}\left(\mathbf{p}_s, t_s'\right)^2/2 = -I_p \tag{2}$$

$$\mathbf{v}\left(\mathbf{p}_s, t_s\right)^2/2 = n\Omega - I_p \tag{3}$$

where n is the harmonic order, t_s', t_s correspond to the ionization and recombination moment of each order harmonics, respectively. The value of t_s', t_s are substituted into the formula of transition dipole matrix elements. The first transition matrix element $\boldsymbol{d}^*(\boldsymbol{V}) = \langle \boldsymbol{V}|\mathbf{r}|0\rangle$ describes the ionization step from a bound state to the plane-wave continuum state and the second one $\boldsymbol{d}(\boldsymbol{V}) = \langle 0|\mathbf{r}|\boldsymbol{V}\rangle$ denotes the recombination step. It is noteworthy that the ionization and recombination of the electron in the electric field take place in complex time according to saddle point equations. It is interpreted that the imaginary part of t_s' is corresponding to the tunneling ionization process and the small imaginary part of t_s is neglectable associated with the electron recombination time.

3. Results and discussion

3.1. Circularly polarized HHG from three-color field

In our simulation, we employ an OTC electric field superposed with a linear polarized gating field as the driving field. Wavelengths of the OTC field components are 800 nm along the X-axis and 1200 nm along the Y-axis respectively, while the wavelength of the associated gating field is 2400 nm. The intensity of each laser field is set to $I_1 = 1.8 \times 10^{14}\mathrm{W/cm^2}$ for 800-nm component, $I_2 = 5.4 \times 10^{13}\mathrm{W/cm^2}$ for 1200-nm component and $I_3 = 2.2 \times 10^{13}\mathrm{W/cm^2}$ for 2400-nm component. The synthesized three-color field can be expressed as

$$\begin{aligned}\boldsymbol{E}(t) =& E_1 f(t)\cos(\omega_1 t + \phi)\hat{\boldsymbol{x}} + E_2 f(t)\cos(\omega_2 t)\hat{\boldsymbol{y}} + E_3 f(t)[\cos(\alpha)\cos(\omega_3(t+\Delta t))\hat{\boldsymbol{x}} \\ &+ \sin(\alpha)\cos(\omega_3(t+\Delta t))\hat{\boldsymbol{y}}]\end{aligned} \tag{4}$$

where E_1, E_2, E_3 and $\omega_1, \omega_2, \omega_3$ are amplitudes and angular frequencies of corresponding electric fields. $f(t)$ is the envelope of the driving pulses. All driving pulses are Gaussian shape with the duration of 40 fs. α is the rotation angle of the gating field polarization and is fixed at 135° from the X-axis. ϕ represents the relative phase of the OTC field and Δt represents the delay time between the fundamental field (800-nm electric field) and the IR gating field. The relative phase ϕ is set to $\pi/2$ and delay time Δt is zero, resulting in a single broken-8-shaped Lissajous figure with a spatiotemporal asymmetry as Fig. 1 presents. The synthesized driving field contains multiple optical cycles and the central part of the pulse, which contributes dominantly to HHG, is highlighted with a bold red line.

The simulation result of HHG is depicted in Fig. 2(a). The intensity of RCP harmonics D_+ (red line) is higher than that of the LCP harmonics D_- (blue line) at the range from the 50th-order to the 77th-order. To clearly present the variation of the harmonic ellipticity, we plot the harmonic-order-dependent ellipticity in Fig. 2(b). Under the 54th order, the absolute value of the ellipticity experiences a big oscillation and is less than 0.5 approximately. In contrast, the harmonic ellipticity rises to 0.8 over the 60th to 69th order due to the great intensity difference between two counter-rotating components of the harmonics in the cutoff region.

By performing inverse Fourier Transforms of the supercontinuum beyond the 58th order, we obtain an isolated attosecond pulse. To reveal the polarization characteristics of the generated attosecond pulses, we present the electric fields of the attosecond pulses in 3D plot as shown

Optics EXPRESS

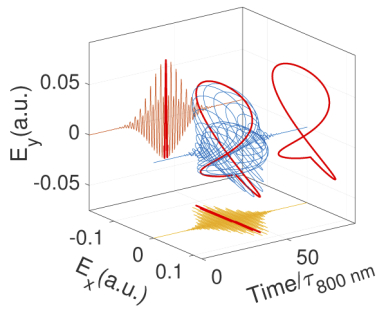

Fig. 1. The 3D plot of the electric field for the three-color laser field. The intensity of the 800-nm pulse is $I_1 = 1.8 \times 10^{14}\mathrm{W/cm^2}$, the intensity of the 1200-nm pulse is $I_2 = 5.4 \times 10^{13}\mathrm{W/cm^2}$ and the intensity of the 2400-nm pulse is $I_3 = 2.2 \times 10^{13}\mathrm{W/cm^2}$. All pulse durations of the three-color field are 40 fs. The central peak of the driving pulse is highlighted with a bold red line.

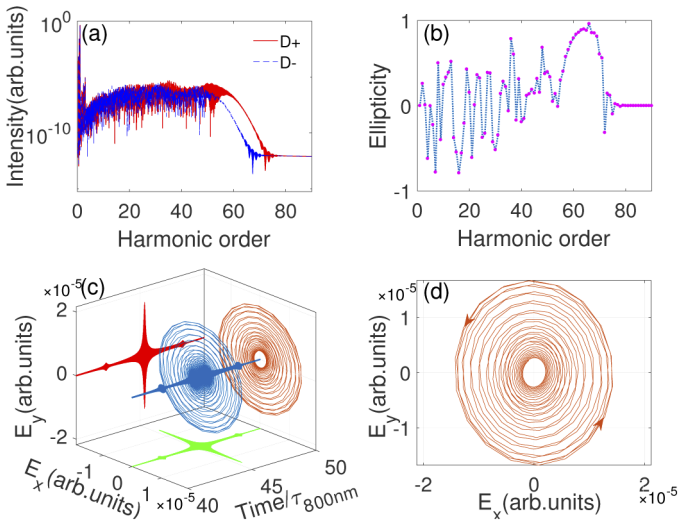

Fig. 2. (a) The harmonic spectrum generated by the three-color driving field. The D_+ harmonic corresponds to red solid line and the D_- harmonic corresponds to blue dashed line. (b) The ellipticity distribution of harmonics as a function of the harmonic order. (c) The 3D plot of the electric field for synthesized pulses via superposing the harmonics beyond the 58th order. (d) The electric field projection of the central attosecond pulse on the polarization plane.

in Fig. 2(c). The main attosecond pulse with a high ellipticity occurs at the central optical cycle (45 $\tau_{800\,\mathrm{nm}}$) of the fundamental field. Besides, there are two tiny satellite peaks at 42 and 48 $\tau_{800\,\mathrm{nm}}$. The amplitude of the satellite peaks is less than that of the main pulse with one order of magnitude. These weak satellite peaks originate from the lower cutoff energy of the harmonic emitted at adjacent optical cycles. Also, the projection of the electric field of the main pulse is present in Fig. 2(d) to clarify the helicity. The arrows indicate that the electric field is counter-clockwise rotating along the time axis.

In addition, we compare the harmonic yield under different driving fields in Fig. 3. We calculate the harmonic spectra of the bichromatic counter-rotating circularly polarized (BCCP) laser pulses and the OTC laser pulses. For the OTC and BCCP schemes, the synthesized field

Optics EXPRESS

consists of the fundamental 1600-nm (ω) and its second harmonic 800-nm (2ω) components. The peak intensity and the intensity ratio $I_{2\omega}/I_{\omega}$ of the OTC and BCCP fields are consistent with the three-color field used in Fig. 2(a). In Fig. 3, it can be seen that the harmonic intensity of the three-color field is comparable with that of the OTC and BCCP fields under the 30th order. From the 30th order to the 50th order, the harmonic spectra of the OTC and BCCP fields start descending, while it is unaltered for the three-color field. Above the 50th order, the harmonic intensity in the three-color field is at least an order of magnitude higher than the others. It indicates that the harmonics driven by the three-color field is enhanced at the cutoff region, which can provide attosecond emissions efficiently.

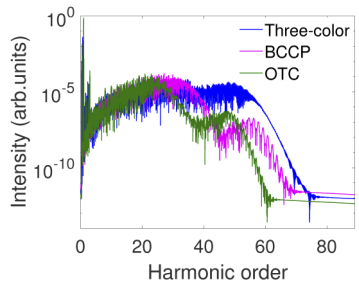

Fig. 3. The HHG spectra driven by different driving lasers. The blue line presents the HHG spectrum of the three-color field in Fig. 2(a). The magenta line presents the HHG spectrum of the bichromatic counter-rotating circularly polarized (BCCP) field. The green line presents the HHG spectrum of the orthogonally polarized two-color (OTC) driving field.

3.2. Classical and quantum trajectory of electrons in three-color field

To analyze the origin of the high harmonic ellipticity from the three-color field, we calculate the electron trajectories and velocities by solving the Newton's motion equations. Then, we investigate the contribution of photoionization and recombination to the HHG through the saddle point analysis.

First, we solve classical motion equations for the three-color driving field. Specifically, we exhibit the results of the 66th order harmonic from the cutoff region due to its highest ellipticity. As shown in Fig. 4(b), the electron travels 50 atomic units away and back along a curved trajectory. Its curved trajectory is different from the electron trajectory driven by a monochromic linearly polarized electric field. In addition, one can see that the acceleration vector of the recombination is almost perpendicular to the acceleration vector of the ionization in Fig. 4(a), which is consistent with the result of Ref. [4].

In comparison, we remove the IR gating component of the three-color driving field and solve the same equations of motion for the remaining OTC field without changing any parameters. We still chose the electron corresponding to the cutoff region. As shown in Fig. 4(e), the electron oscillation is confined to 10 atomic units on X-axis and ±2 atomic units on Y-axis. The trajectory in the OTC field is closed to that of in a monochromic linear field for which results in linearly polarized harmonics. Besides, the acceleration vector of the recombination in Fig. 4(d) is nearly parallel with that of the ionization. Compared to Fig. 4(c) and 4(f), we find that the Lissajous figure of the three-color driving field is similar to that of the OTC field. But the whole Lissajous figure is shifted along the polarized direction of the gating field. This electric field shift in polarization plane makes electrons travel longer in the three-color field and have chance to revisit their parent ion along curved trajectories with extra angular momentum. Therefore, the harmonic from the three-color field has a high ellipticity at the cutoff region.

Optics EXPRESS

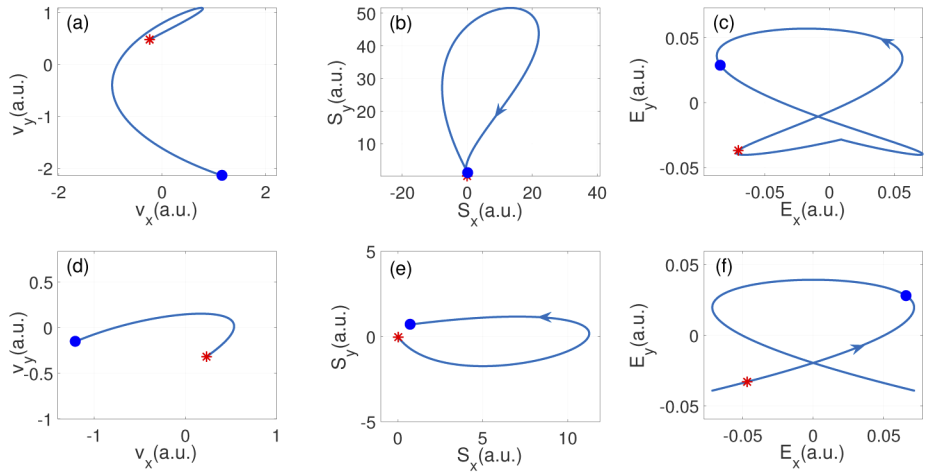

Fig. 4. The solution of the classical motion equations. The initial positions and the recombination positions of the electrons are indicated by blue solid dots and orange asterisks respectively in all figures. The results of the electron, corresponding to the 66th order for the three-color driving field, is chosen to be depicted in panel (a) (b) and (c). (a) The velocity curve of the electron corresponding to the 66th order harmonic, whose ellipticity is highest in Fig. 2(b). (b) The classical trajectory of the electron. (c) The ionization and recombination positions of the electron in the Lissajous figure; The panel (d) (e) (f) are corresponding to the OTC driving field. (d) The classical velocity curve of the electron corresponding to the harmonic located at cutoff region. (e) The classical trajectory of the electron. (f) The ionization and recombination positions of the electron in the Lissajous figure.

Moreover, we perform the time-frequency analysis of the D_+ harmonics for both aforementioned driving fields via the Gabor Transform as depicted in Fig. 5(a) and (b). One can see that, from 42 to 48 $\tau_{800\,\mathrm{nm}}$, there are three harmonic emittings (P_1, P_2 and P_3) for the three-color field. The central emitting P_2 is separated by 3 $\tau_{800\,\mathrm{nm}}$ from the adjacent emitting P_1 and P_3. On the other hand, five harmonic emittings (R_1 to R_5 in Fig. 5(b)) exist for the OTC field in the same time range. The time interval between each harmonic emitting is 1.5 $\tau_{800\,\mathrm{nm}}$. Hence, the spatiotemporal asymmetry induced by the superimposition of the OTC field upon the IR gating field can extend the time interval between two harmonic emittings. Note that the similar time interval is 0.5 $\tau_{800\,\mathrm{nm}}$ for the HHG from the 800-nm linear driving pulse. And the pulse duration of the driving lasers is required to less than 7 fs to produce the isolated attosecond pulse. With the time interval increasing by 6 times, all pulse durations of the three-color driving field can be prolonged by 6 times as well, i.e. to 40 fs. This effect of extending pulse duration is similar to the GDOG method used in the linearly polarized attosecond pulse generation. Thus, the multi-cycle lasers can be applied to generate the isolated attosecond pulse.

To analyze the contributions of each ionization and recombination matrix elements, we employ the saddle point method outlined in Sec.2. We calculate the individual ionization matrix elements $d_{ion,p_\pm}$ and the recombination matrix elements $d^{\pm}_{rec,p_\pm}$ for initial $p_\pm$ orbitals. Recombination matrix elements are projected on the relevant polarization vector $\boldsymbol{e}_\pm = \frac{1}{\sqrt{2}}(\boldsymbol{e}_x \pm i\boldsymbol{e}_y)$ and the total induced dipole moment is obtained from the product of the ionization and the recombination matrix elements. The total induced dipole moments with same polarization vector from the $p_\pm$ orbitals are summed coherently. The magnitudes of the total induced dipole moment for the harmonics of $\boldsymbol{e}_+$ polarization (red solid line) and $\boldsymbol{e}_-$ polarization (blue solid line) are present in Fig. 6(a). The dominant emission with $\boldsymbol{e}_+$ polarization occurs in the range over the cutoff region, which is consistent with the result calculated by SFA. These results are influenced by the relative phase

Optics EXPRESS

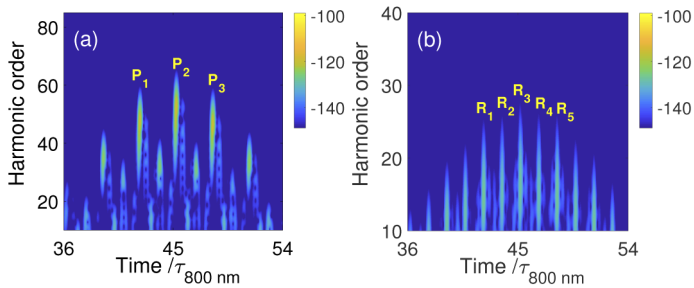

Fig. 5. (a) The time-frequency analysis of the D_+ component of the harmonic spectrum generated by the three-color driving field. (b) The time-frequency analysis of the D_+ component of the harmonic spectrum generated by the OTC field, whose other optical parameters are identical to that of the three-color driving field.

between total induced dipole moments originated from the p_+ or p_- orbitals. From the 36th order to the 50th order, the relative phase for two polarization vectors $\boldsymbol{e}_\pm$ have an identical variation around $\pi/2$ as Fig. 6(b) depicts. In consequence, a constructive interference between emissions from the p_+ and p_- orbitals occurs for both polarization vectors and the emission of harmonics rises up at the cutoff region. But from the 50th order to the 60th order, the relative phase for $\boldsymbol{e}_-$ polarization jumps to π so that destructive interference occurs for the LCP harmonics. In contrast, the constructive interference is maintained with the relative phase for $\boldsymbol{e}_+$ polarization varying around $\pi/2$. Its constructive interference leads to a stronger emission for the RCP harmonics. These effects result in extending harmonic orders of the cutoff for the D_+ harmonics compared to that of the D_+ harmonics, as shown in Fig. 2(a).

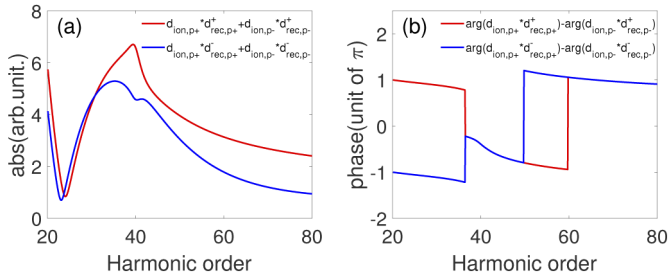

Fig. 6. (a) Total induced dipole matrix elements corresponding to the 66th order harmonic generated by the three-color field, the matrix element for $\boldsymbol{e}_+$ polarization vector corresponds to red line and the matrix element for $\boldsymbol{e}_-$ polarization vector corresponds to blue line. (b)The relative phase between each component of total induced dipole matrix elements.

3.3. *Robustness analyses of HHG and isolated circularly attosecond pulses generation*

In this section, we investigate the robustness of the three-color field scheme and manifest that an isolated circular attosecond pulse can be obtained by adjusting intensity ratios. First, we analyze the relative-phase-dependent robustness of HHG. The harmonic ellipticity and total intensity distribution as a function of relative phase ϕ are presented in Fig. 7(a) and (b), respectively. The absolute value of ellipticity at the cutoff region is beyond 0.8 in the range from $\phi = 0.3\pi$ to $\phi = 0.7\pi$. With the relative phase ϕ changing, the cutoff energy varies as shown in Fig. 7(b). But the harmonics at the high ellipticity region are as intense as that of at the plateau region regardless of the relative phase ϕ varying.

Optics EXPRESS

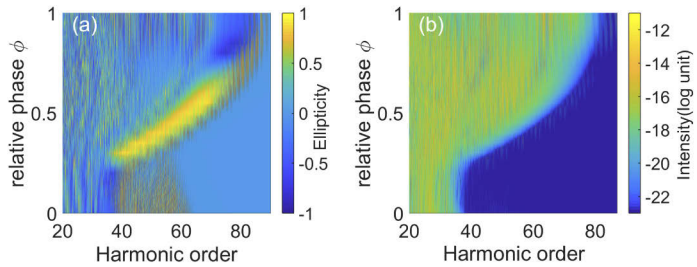

Fig. 7. (a) The ellipticity distribution as a function with the relative phase Φ of the OTC field. (b) The total harmonic intensity distribution as a function with the relative phase Φ of the OTC field. The harmonic intensity is present in the logarithmic unit.

Moreover, we analyze the ellipticity distribution of high harmonics as a function of delay Δt between the OTC field and the IR gating field. In Fig. 8, the ellipticity distribution appears the high sensitivity to the delay Δt. The high ellipticity at the cutoff region merely occurs around $n\tau_0$ (τ_0 is identical to the optical period of the 2400-nm wavelength, n is the integer). We also investigate the ellipticity dependence on intensity ratios of three driving pulses on which the fundamental field is intensity-fixed. While the intensity ratio rises, the harmonics at the cutoff region remain the high ellipticity and the cutoff energy translates towards the higher energy as a consequence of the cutoff law.

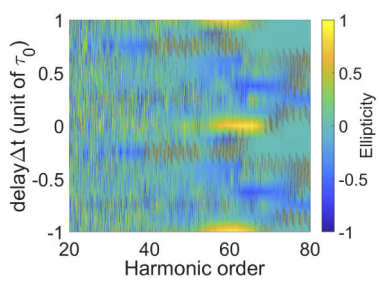

Fig. 8. The ellipticity distribution as a function with the time delay Δt between the fundamental field and the IR gating field.

To suppress satellite pulses on two sides of the main pulse, we fix the intensity of the fundamental electric field and increase the intensity of two other electric fields. The intensity of the 1200-nm and the 2400-nm electric field are increased to $9\times10^{13}\mathrm{W/cm^2}$ and $3.65\times10^{13}\mathrm{W/cm^2}$, respectively. With the intensity ratio of the laser field increasing, the cutoff order of the main emitting P_2 rises to the 97th order but that of the adjacent emittings P_1, P_3 only rises to the 87th orders as shown in Fig. 9(a). The cutoff difference is extended from 5 harmonic order to 10 harmonic order. In consequence, by superposing the harmonic beyond the 87th order, satellite pulses can be suppressed strongly and only the main pulse is left. As shown in Fig. 9(b), an isolated circular attosecond pulse is generated by the three-color driving field. We also calculate the ellipticity of the attosecond pulses and the value is 0.936. The result illustrates that the three-color electric field enables us to generate an isolated attosecond pulse with high ellipticity by adjusting the intensity ratio between driving field components. In addition, since the effective pulse duration is dependent on the shortest duration among three driving pulses, it is anticipated that the duration of the 1200-nm and the 2400-nm pulses can be further extended as long as the 800-nm pulse keeps the duration of 40 fs.

Optics EXPRESS

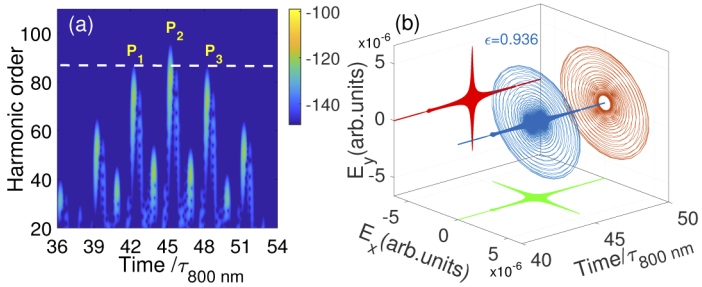

Fig. 9. (a) The time-frequency analysis of the D_+ component of the harmonic spectrum from the three-color driving field with the intensity of the 1200-nm and 2400-nm components increasing. The dashed line indicates the 87th harmonic order. (b) The 3D plot of the electric field for the synthesized isolated attosecond pulse with a high ellipticity of 0.936.

4. Conclusion

In conclusion, we theoretically analyze the HHG in the three-color laser field for isotropic atomic media and demonstrate the possibility to generate an isolated attosecond pulse with high ellipticity. The three-color driving field is synthesized by an OTC laser field with a linearly polarized gating field. The IR gating field imposes a transversal shift for the OTC electric field in the polarization plane and extends the time interval between adjacent harmonic emittings. The gating-field induced peculiarity offers a unique opportunity for multi-cycle fields to generate the circular attosecond pulses. In the simulation, by adjusting the intensity ratio between the three-color field components, we obtain an isolated attosecond pulse with a high ellipticity of 0.936. We envisage that this property can remove the facility restrictions from requirements of few-cycle driving pulses for isolated circular attosecond pulse generation.

Funding

National key research and development program (2017YFE0116600); National Natural Science Foundation of China (11627809, 11874165, 11934006, 91950202); Science and Technology Planning Project of Guangdong Province (2018B090944001).

Acknowledgments

Numerical simulations presented in this paper were carried out using the High Performance Computing Center experimental testbed in SCTS/CGCL (see http://grid.hust.edu.cn/hpcc).

Disclosures

The authors declare no conflicts of interest.

References

1. A. D. Bandrauk and K.-J. Yuan, "Circularly polarised attosecond pulses: generation and applications," Mol. Phys. **114**(3-4), 344–355 (2016).
2. B. Thole, P. Carra, F. Sette, and G. van der Laan, "X-ray circular dichroism as a probe of orbital magnetization," Phys. Rev. Lett. **68**(12), 1943–1946 (1992).
3. O. Kfir, P. Grychtol, E. Turgut, R. Knut, D. Zusin, D. Popmintchev, T. Popmintchev, H. Nembach, J. M. Shaw, and A. Fleischer, "Generation of bright phase-matched circularly-polarized extreme ultraviolet high harmonics," Nat. Photonics **9**(2), 99–105 (2015).
4. D. Baykusheva, M. S. Ahsan, N. Lin, and H. J. Wörner, "Bicircular high-harmonic spectroscopy reveals dynamical symmetries of atoms and molecules," Phys. Rev. Lett. **116**(12), 123001 (2016).
5. L. Li, P. Lan, L. He, W. Cao, Q. Zhang, and P. Lu, "Determination of electron band structure using temporal interferometry," Phys. Rev. Lett. **124**(15), 157403 (2020).

Optics EXPRESS

6. D. D. Hickstein, F. J. Dollar, P. Grychtol, J. L. Ellis, R. Knut, C. Hernández-García, D. Zusin, C. Gentry, J. M. Shaw, T. Fan, K. M. Dorney, A. Becker, A. Jaroń-Becker, H. C. Kapteyn, M. M. Murnane, and C. G. Durfee, "Non-collinear generation of angularly isolated circularly polarized high harmonics," Nat. Photonics **9**(11), 743–750 (2015).
7. F. Siegrist, J. A. Gessner, M. Ossiander, C. Denker, Y. P. Chang, M. C. Schroder, A. Guggenmos, Y. Cui, J. Walowski, U. Martens, J. K. Dewhurst, U. Kleineberg, M. Munzenberg, S. Sharma, and M. Schultze, "Light-wave dynamic control of magnetism," Nature **571**(7764), 240–244 (2019).
8. X. Zhang, L. Li, X. Zhu, K. Liu, X. Liu, D. Wang, P. Lan, I. Barth, and P. Lu, "Subpetahertz helicity-modulated high-order harmonic radiation," Phys. Rev. A **98**(2), 023418 (2018).
9. M. Hentschel, R. Kienberger, C. Spielmann, G. A. Reider, N. Milosevic, T. Brabec, P. Corkum, U. Heinzmann, M. Drescher, and F. Krausz, "Attosecond metrology," Nature **414**(6863), 509–513 (2001).
10. T. Gaumnitz, A. Jain, Y. Pertot, M. Huppert, I. Jordan, F. Ardana-Lamas, and H. J. Wörner, "Streaking of 43-attosecond soft-X-ray pulses generated by a passively relative phase-stable mid-infrared driver," Opt. Express **25**(22), 27506–27518 (2017).
11. M. Hentschel, R. Kienberger, C. Spielmann, G. A. Reider, and F. Krausz, "Attosecond metrology," Nature **414**(6863), 509–513 (2001).
12. G. Sansone, E. Benedetti, F. Calegari, C. Vozzi, L. Avaldi, R. Flammini, L. Poletto, P. Villoresi, C. Altucci, R. Velotta, S. Stagira, S. De Silvestri, and M. Nisoli, "Isolated single-cycle attosecond pulses," Science **314**(5798), 443–446 (2006).
13. E. J. Takahashi, P. Lan, O. D. Muecke, Y. Nabekawa, and K. Midorikawa, "Infrared Two-Color Multicycle Laser Field Synthesis for Generating an Intense Attosecond Pulse," Phys. Rev. Lett. **104**(23), 233901 (2010).
14. H. Mashiko, S. Gilbertson, C. Li, S. D. Khan, M. M. Shakya, E. Moon, and Z. Chang, "Double optical gating of high-order harmonic generation with carrier-envelope phase stabilized lasers," Phys. Rev. Lett. **100**(10), 103906 (2008).
15. X. Feng, S. Gilbertson, H. Mashiko, H. Wang, S. D. Khan, M. Chini, Y. Wu, K. Zhao, and Z. Chang, "Generation of isolated attosecond pulses with 20 to 28 femtosecond lasers," Phys. Rev. Lett. **103**(18), 183901 (2009).
16. B. Vodungbo, A. B. Sardinha, J. Gautier, G. Lambert, C. Valentin, M. Lozano, G. Iaquaniello, F. Delmotte, S. Sebban, and J. Lüning, "Polarization control of high order harmonics in the EUV photon energy range," Opt. Express **19**(5), 4346–4356 (2011).
17. F. Willems, C. Smeenk, N. Zhavoronkov, O. Kornilov, I. Radu, M. Schmidbauer, M. Hanke, C. von Korff Schmising, M. Vrakking, and S. Eisebitt, "Probing ultrafast spin dynamics with high-harmonic magnetic circular dichroism spectroscopy," Phys. Rev. B **92**(22), 220405 (2015).
18. K.-J. Yuan and A. D. Bandrauk, "Single circularly polarized attosecond pulse generation by intense few cycle elliptically polarized laser pulses and terahertz fields from molecular media," Phys. Rev. Lett. **110**(2), 023003 (2013).
19. C. Hernández-García, C. Durfee, D. Hickstein, T. Popmintchev, A. Meier, M. Murnane, H. Kapteyn, I. Sola, A. Jaron-Becker, and A. Becker, "Schemes for generation of isolated attosecond pulses of pure circular polarization," Phys. Rev. A **93**(4), 043855 (2016).
20. L. Medisauskas, J. Wragg, H. van der Hart, and M. Y. Ivanov, "Generating Isolated Elliptically Polarized Attosecond Pulses Using Bichromatic Counterrotating Circularly Polarized Laser Fields," Phys. Rev. Lett. **115**(15), 153001 (2015).
21. A. Ferré, C. Handschin, M. Dumergue, F. Burgy, A. Comby, D. Descamps, B. Fabre, G. Garcia, R. Géneaux, and L. Merceron, "A table-top ultrashort light source in the extreme ultraviolet for circular dichroism experiments," Nat. Photonics **9**(2), 93–98 (2015).
22. A. Fleischer, O. Kfir, T. Diskin, P. Sidorenko, and O. Cohen, "Spin angular momentum and tunable polarization in high-harmonic generation," Nat. Photonics **8**(7), 543–549 (2014).
23. F. Mauger, A. Bandrauk, and T. Uzer, "Circularly polarized molecular high harmonic generation using a bicircular laser," J. Phys. B: At., Mol. Opt. Phys. **49**(10), 10LT01 (2016).
24. K.-J. Yuan and A. D. Bandrauk, "Above-threshold ionization in molecules by intense multiple-frequency circularly polarized laser pulses," Phys. Rev. A **98**(2), 023413 (2018).
25. D. Milošević, "Circularly polarized high harmonics generated by a bicircular field from inert atomic gases in the p state: A tool for exploring chirality-sensitive processes," Phys. Rev. A **92**(4), 043827 (2015).
26. L. Li, P. Lan, L. He, X. Zhu, J. Chen, and P. Lu, "Scaling Law of High Harmonic Generation in the Framework of Photon Channels," Phys. Rev. Lett. **120**(22), 223203 (2018).
27. D. Shafir, Y. Mairesse, H. J. Wörner, K. Rupnik, D. M. Villeneuve, P. B. Corkum, and N. Dudovich, "Probing the symmetry of atomic wavefunctions from the point of view of strong field-driven electrons," New J. Phys. **12**(7), 073032 (2010).
28. G. Lambert, B. Vodungbo, J. Gautier, B. Mahieu, V. Malka, S. Sebban, P. Zeitoun, J. Luning, J. Perron, and A. Andreev, "Towards enabling femtosecond helicity-dependent spectroscopy with high-harmonic sources," Nat. Commun. **6**(1), 6167 (2015).
29. K. M. Dorney, J. L. Ellis, C. Hernández-García, D. D. Hickstein, C. A. Mancuso, N. Brooks, T. Fan, G. Fan, D. Zusin, and C. Gentry, "Helicity-selective enhancement and polarization control of attosecond high harmonic waveforms driven by bichromatic circularly polarized laser fields," Phys. Rev. Lett. **119**(6), 063201 (2017).
30. C. Zhai, R. Shao, P. Lan, B. Wang, Y. Zhang, H. Yuan, S.M. Njoroge, L. He, and P. Lu, "Ellipticity control of high-order harmonic generation with nearly orthogonal two-color laser fields," Phys. Res. A **101**, 053407 (2020).

Optics EXPRESS

31. B. Mahieu, S. Stremoukhov, D. Gauthier, C. Spezzani, C. Alves, B. Vodungbo, P. Zeitoun, V. Malka, G. De Ninno, and G. Lambert, "Control of ellipticity in high-order harmonic generation driven by two linearly polarized fields," Phys. Rev. A **97**(4), 043857 (2018).
32. M.-Z. Li, Y. Xu, G.-R. Jia, and X.-B. Bian, "Controlling polarization of high-order harmonic generation by molecular alignment in a bicircular laser field," Phys. Rev. A **100**(3), 033410 (2019).
33. C. Zhai, R. Shao, P. Lan, B. Wang, Y. Zhang, H. Yuan, S. M. Njoroge, L. He, and P. Lu, "Ellipticity control of high-order harmonic generation with nearly orthogonal two-color laser fields," *Phys. Rev. A.* in press.
34. D. Baykusheva, S. Brennecke, M. Lein, and H. J. Worner, "Signatures of Electronic Structure in Bicircular High-Harmonic Spectroscopy," Phys. Rev. Lett. **119**(20), 203201 (2017).
35. A. Jimenezgalan, N. Zhavoronkov, D. Ayuso, F. Morales, S. Patchkovskii, M. Schloz, E. Pisanty, O. Smirnova, and M. Ivanov, "Control of attosecond light polarization in two-color bicircular fields," Phys. Rev. A **97**(2), 023409 (2018).
36. P.-C. Huang, C. Hernández-García, J.-T. Huang, P.-Y. Huang, C.-H. Lu, L. Rego, D. D. Hickstein, J. L. Ellis, A. Jaron-Becker, and A. Becker, "Polarization control of isolated high-harmonic pulses," Nat. Photonics **12**(6), 349–354 (2018).
37. D. Azoury, O. Kneller, M. Krüger, B. D. Bruner, O. Cohen, Y. Mairesse, and N. Dudovich, "Interferometric attosecond lock-in measurement of extreme-ultraviolet circular dichroism," Nat. Photonics **13**(3), 198–204 (2019).
38. K. Schafer, B. Yang, L. DiMauro, and K. Kulander, "Above threshold ionization beyond the high harmonic cutoff," Phys. Rev. Lett. **70**(11), 1599–1602 (1993).
39. M. Lewenstein, P. Balcou, M. Y. Ivanov, A. L'huillier, and P. B. Corkum, "Theory of high-harmonic generation by low-frequency laser fields," Phys. Rev. A **49**(3), 2117–2132 (1994).
40. P. Antoine, B. Carré, A. L'Huillier, and M. Lewenstein, "Polarization of high-order harmonics," Phys. Rev. A **55**(2), 1314–1324 (1997).
41. K. Amini, J. Biegert, F. Calegari, A. Chacón, M. F. Ciappina, A. Dauphin, D. K. Efimov, C. F. de Morisson Faria, K. Giergiel, and P. Gniewek, "Symphony on strong field approximation," Rep. Prog. Phys. **82**(11), 116001 (2019).
42. D. B. Milosevic, W. Becker, and R. Kopold, "Generation of circularly polarized high-order harmonics by two-color coplanar field mixing," Phys. Rev. A **61**(6), 063403 (2000).
43. M. Y. Ivanov, T. Brabec, and N. Burnett, "Coulomb corrections and polarization effects in high-intensity high-harmonic emission," Phys. Rev. A **54**(1), 742–745 (1996).
44. D. Ayuso, A. Jiménez-Galán, F. Morales, M. Ivanov, and O. Smirnova, "Attosecond control of spin polarization in electron–ion recollision driven by intense tailored fields," New J. Phys. **19**(7), 073007 (2017).
45. J. Tate, T. Auguste, H. G. Muller, P. Salieres, P. Agostini, and L. F. Dimauro, "Scaling of wave-packet dynamics in an intense midinfrared field," Phys. Rev. Lett. **98**(1), 013901 (2007).